DISCLAIMER

U.S. DEPARTMENT OF ENERGY

PNNL-38365

Prepared for the U.S. Department of Energy
under Contract DE-AC05-76RL01830

Effects of dose rate on the microstructure and deuterium retention in γ-$LiAlO_2$ pellets

Weilin Jiang
Andrew M. Casella
David J. Senor

Final Report
Tritium Modernization Program
September 2025

Pacific Northwest
NATIONAL LABORATORY

Proudly Operated by Battelle *Since 1965*

Effects of dose rate on the microstructure and deuterium retention in γ-$LiAlO_2$ pellets

Weilin Jiang, Andrew M. Casella, David J. Senor
PNNL Contributors: Libor Kovarik, Zihua Zhu, Xin Zhang, Xiaoxu Li, Karen Kruska
Texas A&M University Contributors: Zhihan Hu, Lin Shao

Summary

This report presents experimental findings obtained from November 2024 to September 2025. Defect accumulation and microstructural evolution during ion irradiation at elevated temperatures are governed by two competing processes: defect production, driven by dose rate, and defect recovery, controlled by defect diffusion, interaction, and annihilation. At a given dose, the resulting microstructural evolution depends on both the dose rate and irradiation temperature. As a continuation of our FY24 tritium science project, which investigated temperature effects at a fixed dose rate, this study focuses on dose-rate effects at a fixed temperature to provide deeper insights into the irradiated microstructure and compositional changes in γ-$LiAlO_2$ pellets. The study aims to elucidate the impact of dose rate on microstructure, precipitate morphology, deuterium retention, and lithium volatility in γ-$LiAlO_2$ pellets under sequential 120 keV He^+ and 80 keV D_2^+ ion irradiation. Three dose rates of 7.3×10^{-4}, 2.9×10^{-4} and 6.8×10^{-5} dpa/s were applied to achieve the same total ion fluence of 2×10^{17} $(He^+ + D^+)/cm^2$ at 500 °C, corresponding to a maximum combined dose of 7.55 dpa at ~255 nm. The irradiated pellets were subsequently characterized using scanning transmission electron microscopy (STEM) and time-of-flight secondary ion mass spectrometry (ToF-SIMS).

The microstructural response of γ-$LiAlO_2$ to ion irradiation was found to be strongly dose-rate dependent. At medium and high dose rates, irradiation produced a surface amorphized layer and an underlying crystalline layer containing $LiAl_5O_8$ precipitates, with implanted gases accumulating and forming blisters at the crystalline–amorphous interface. It remains to be investigated whether the amorphized layer was produced by He^+ ion irradiation prior to D_2^+ ion irradiation. In contrast, at low dose rates, the material remained crystalline, with cavities, likely gas-filled, distributed around precipitates, within the γ-$LiAlO_2$ matrix, and along grain boundaries. While precipitate morphology exhibited anisotropy, their size showed little sensitivity to dose rate in the applied range of this study. This result, however, does not rule out the possibility that further reductions in dose rate could influence precipitate size. High dose-rate irradiation enhanced protonium–deuterium isotopic exchange and lithium depletion in the amorphized region. Collectively, the results show that dose rate governs amorphization, gas redistribution, isotopic exchange, and lithium depletion, providing important insights into the mechanisms underlying structural evolution in γ-$LiAlO_2$ pellets under reactor-relevant irradiation conditions.

Table of Contents

1. Introduction

Major microstructural features and gas transport behaviors observed in neutron-irradiated γ-$LiAlO_2$ pellets, including precipitates surrounded by cavities [1], denuded zones along grain boundaries [2], cavity aggregation at boundaries [2], and isotopic exchange between mobile H and trapped D [3], have been successfully reproduced through sequential irradiation with energetic He^+ and D_2^+ ions at elevated temperatures [1-5]. As detailed in our FY24 tritium science report [6], defect accumulation and microstructural evolution during ion irradiation are governed by two competing processes: (1) defect production, driven by dose rate, and (2) defect recovery, controlled by defect diffusion, interaction, and annihilation at elevated temperatures. For a given dose, both irradiation temperature and dose rate are critical in determining the resulting microstructural and compositional changes.

In FY24, we investigated the effects of temperature on the microstructural features in γ-$LiAlO_2$ pellets sequentially irradiated with He^+ and D_2^+ ions at a fixed dose rate. The study [6] revealed that $LiAl_5O_8$ precipitates begin to form at 400 °C, with large, faceted precipitates appearing at 500 °C, as illustrated in Fig. 1. Notably, precipitates formed during ion irradiation at 500 °C exhibited the same crystal structure with comparable compositions as those in neutron-irradiated samples at ~300 °C [2], but were an order of magnitude smaller. The dose rate of ion irradiation is typically 2–4 orders of magnitude higher than neutron irradiation [7]. Such elevated dose rates can generate more complex defect structures, potentially creating deeper trapping sites for migrating atoms, including lithium and implanted gaseous species. Consequently, higher temperatures may be required to release these trapped atoms, facilitating atomic diffusion, defect recovery, and new phase precipitation.

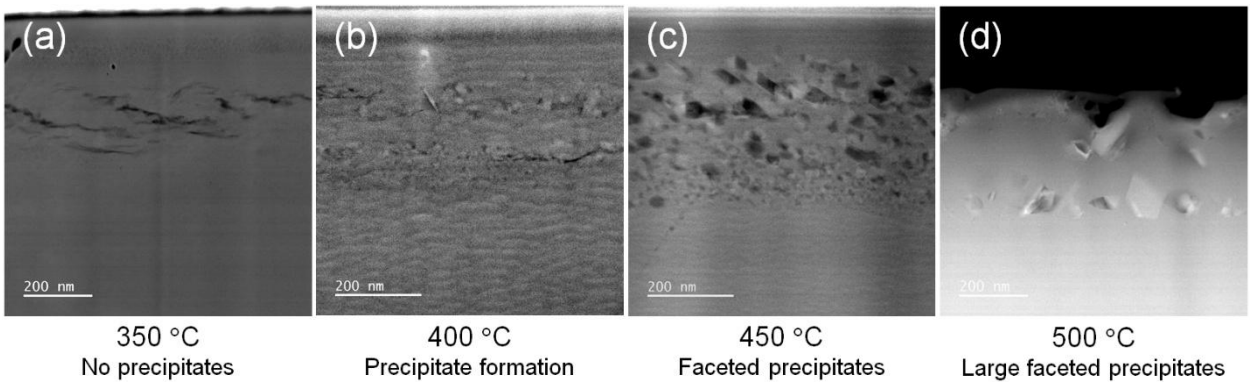

Figure 1. STEM micrographs of the microstructures of γ-$LiAlO_2$ pallets irradiated to 3×10^{17} $(He^+ + D^+)/cm^2$ at (a) 350 °C, (b) 400 °C, (c) 450 °C, and (d) 500 °C. Ion flux: ~3×10^{13} $(ions/cm^2)/sec$; dose rate: ~10^{-3} dpa/sec.

As discussed in a separate study [8], dose-rate effects arise only when defects, primarily point defects, from different damage cascades spatially overlap and either interact to form stable defect clusters (e.g., dislocation loops or voids) or annihilate through recombination with opposite defects. A physical model [8] predicts that, at a fixed temperature, higher dose rates increase the probability of such defect-defect interactions between successive and subsequent cascades. Building on this framework, the present study investigates potential dose-rate effects on microstructural features, deuterium retention, and lithium volatility in γ-$LiAlO_2$ pellets irradiated to a given dose at elevated temperature.

2. Experimental Procedures

2.1. SRIM simulation

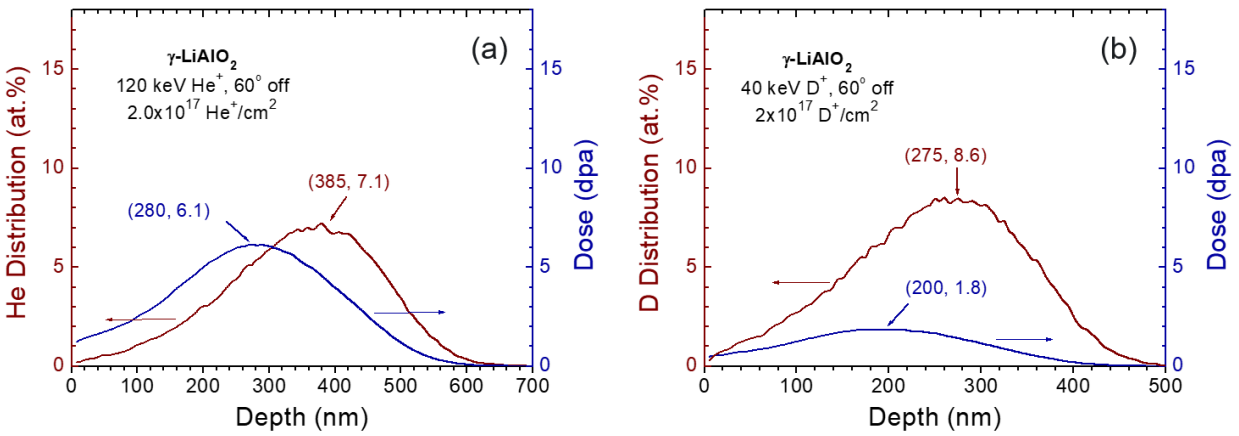

Figure 2. Depth profiles of the atomic percentages and doses from SRIM13 simulations for (a) 120 keV He^+ and (b) 40 keV D^+ ion irradiations of γ-$LiAlO_2$ at 60° off normal to a fluence of 2×10^{17} ions/cm^2.

Table 1. SRIM13 simulation results and dose rates for ion irradiation of γ-$LiAlO_2$ at 500 °C to a total fluence of 2×10^{17} (He^++D^+)/cm^2 at 60° off surface normal.

Sample ID	Ion Beam	Dose Rate (dpa/s)	Damage Peak (nm)	Dose (dpa)	Concentration Peak (nm)	Concentration (at.% He or D)
LDR	120 keV He^+	6.8×10^{-5}	280	6.1	385	7.1
	80 keV D_2^+		200	1.8	275	8.6
MDR	120 keV He^+	2.9×10^{-4}	280	6.1	385	7.1
	80 keV D_2^+		200	1.8	275	8.6
HDR	120 keV He^+	7.3×10^{-4}	280	6.1	385	7.1
	80 keV D_2^+		200	1.8	275	8.6

2×10^{17} (He^++D^+)/cm^2 corresponds to ~13 at.% ^{6}Li burnup in γ-$^6LiAlO_2$ irradiated with a thermalized fission neutron spectrum. 80 keV D_2^+ molecular ions are equivalent to 40 keV D^+ ions that were used for SRIM13 simulations. LDR: Low Dose Rate; MDS: Medium Dose Rate; HDR: High Dose Rate.

To emulate the trapping of deuterium atoms (as a surrogate for tritium) at defect sites produced by He^+ ion irradiation, a sequential irradiation scheme with first He^+ and then D^+ ions was designed such that the implanted D concentration profile spatially overlaps with the He-induced damage profile. Consistent with our earlier work, SRIM13 (Stopping and Range of Ions in Matter, version 2013) simulations [9] were performed to guide the experimental design. The simulations were carried out for 120 keV He^+ ions and 40 keV D^+ ions incident at 60° into γ-$LiAlO_2$, and the calculated results for an ion fluence of 2×10^{17} ions/cm^2 are shown in Fig. 2. This irradiation condition yields He and D concentrations comparable to

those produced in γ-$^6LiAlO_2$ pellets exposed to a thermalized fission neutron spectrum at ~300 °C with a total ^6Li burnup of ~13 at.% [4].

To minimize artificial surface damage effects from energetic light ions, the "monolayer collision step/surface sputtering" option in SRIM13 was employed. The adopted threshold displacement energies were E_d(Li) = 22 eV, E_d(Al) = 84 eV, and E_d(O) = 37 eV, values taken from molecular dynamics (MD) simulations [10]. The surface binding energies were set equal to the corresponding threshold displacement energies for each sublattice. The resulting SRIM13 predictions of peak displacements per atom (dpa) and implanted ion concentrations are summarized in Table 1. For He^+ ion irradiation, the peak dose reaches 6.1 dpa at a depth of ~280 nm, with a peak He concentration of 7.1 at.% at ~385 nm. For D^+ ion irradiation, the peak dose is 1.8 dpa at ~200 nm, with a peak D concentration of 8.6 at.% at ~275 nm. The maximum combined dose is 7.55 dpa at ~255 nm. As intended, the implanted D profile is well aligned with the region of He^+ ion irradiation-induced damage, ensuring that deuterium atoms are introduced directly into defect-rich zones and enabling effective emulation of tritium trapping at He^+ ion-irradiation-induced defect structures in γ-$LiAlO_2$.

2.2. Sequential ion irradiation

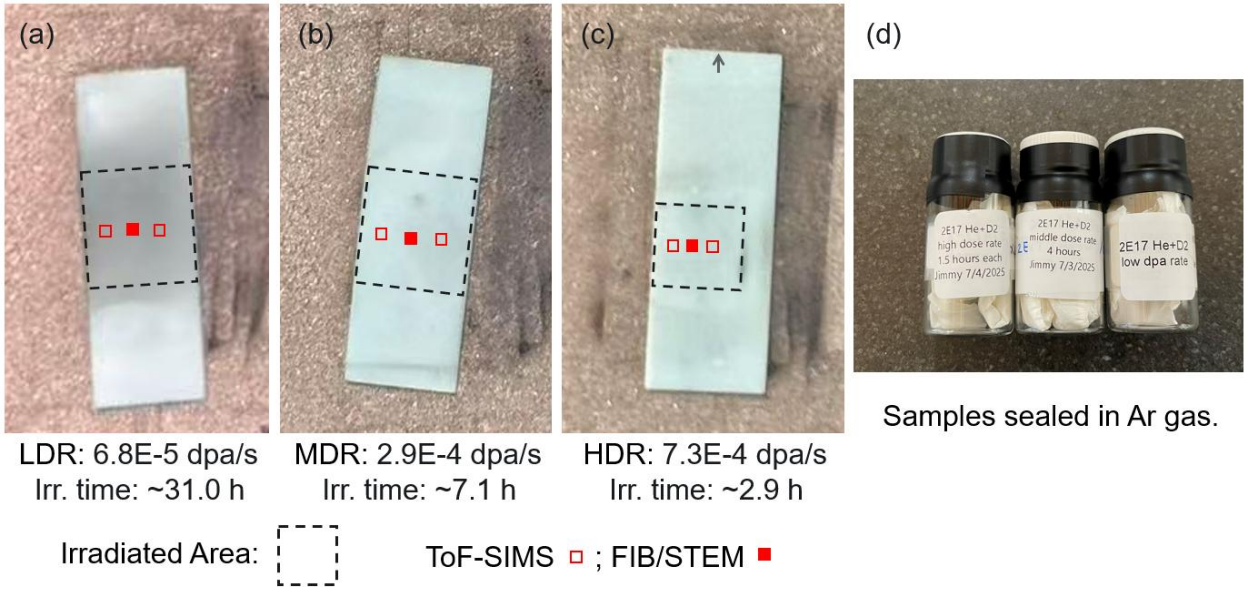

Figure 3. γ-$LiAlO_2$ pellet samples irradiated to 2×10^{17} $(He^+ + D^+)/cm^2$ at 500 °C with dose rates of (a) 6.8×10^{-5}, (b) 2.9×10^{-4} and (c) 7.3×10^{-4} dpa/s. (d) Samples in vials filled with Ar and secured with tape.

Ion irradiation experiments were carried out using a 140 kV ion accelerator equipped with a magnetic rastering system. Sequential irradiation was performed at an incidence angle of 60° relative to the surface normal using 120 keV He^+ ions and 80 keV D_2^+ ions. The total ion fluence was 2×10^{17} $(He^+ + D^+)/cm^2$ at a specimen temperature of 500 °C under three different dose rates: 6.8×10^{-5}, 2.9×10^{-4} and 7.3×10^{-4} dpa/s, corresponding to irradiation times of ~31, ~7.1 and ~2.9 h. These conditions define the low-, medium-, and high-dose-rate cases (LDR, MDR, and HDR, respectively), as summarized in Table 1.

The sequential irradiation was designed such that He^+ ion irradiation was performed first to generate a distribution of displacement defects over a depth range, followed by D^+ ion implantation in the same depth region. This arrangement allowed implanted deuterium atoms (a tritium surrogate) to interact with and become trapped at the stable He-induced defect structures. To achieve a high deuterium flux, a D_2^+ molecular beam was employed instead of a D^+ ion beam. Upon entering the solid, each 80 keV D_2^+ molecular ion dissociates into two 40 keV D^+ ions of equal kinetic energy, thereby producing the equivalent irradiation conditions while doubling the particle flux. Low ion energies and a tilted incidence geometry were deliberately selected to facilitate subsequent depth profiling of implanted species and damage distributions. Beam rastering was applied to ensure spatial uniformity of irradiation over the targeted area. Irradiations were manually paused approximately every 15 minutes for beam current checks, with the values arithmetically averaged over each interval to estimate the dose rate. Despite this procedure, the total ion fluence is subject to an uncertainty of ~10% or higher. The pellets were heated to 500 °C prior to irradiation using a filament positioned behind a copper holder. The irradiated pellets and the marked locations selected for post-irradiation characterization are shown in Figs. 3(a) –3(c). After irradiation, the γ-$LiAlO_2$ pellets were carefully handled to prevent material degradation. Each pellet sealed inside a glass vial filled with Ar gas and secured with tape, as shown in Fig. 3(d).

2.3. Characterization of irradiated samples

Cross-sectional scanning transmission electron microscopy (STEM) specimens of irradiated γ-$LiAlO_2$ pellets were prepared using an FEI Helios 600 Nanolab dual-beam focused ion beam (FIB) system. To protect the surface regions of interest from ion beam damage during milling, ~300 nm of electron-beam–deposited platinum was first applied, followed by ~4 μm of ion-beam–deposited carbon. Standard Ga^+ ion beam "lift-out" procedures were then used to extract site-specific lamellae, which were subsequently mounted onto copper support grids. The lamellae were thinned using progressively lower Ga^+ accelerating voltages, with the final thinning performed at 5 kV to a thickness of ~100 nm, ensuring electron transparency while minimizing Ga^+ irradiation damage.

The specimens were examined in a ThermoFisher Scientific aberration-corrected Spectra Ultra STEM operated at 300 kV. High-angle annular dark-field (HAADF) STEM imaging was employed to image irradiated microstructures. To mitigate electron beam–induced damage and minimize sample heating, low-dose imaging conditions were used, with a beam current of 20 pA, a dwell time of ~1 μs per pixel, and frame averaging over ~20 sequentially acquired, spatially overlapping images. This acquisition strategy improved the signal-to-noise ratio while preserving microstructural integrity.

Chemical depth profiling was performed on irradiated γ-$LiAlO_2$ pellets by time-of-flight secondary ion mass spectrometry (ToF-SIMS) using a TOF.SIMS5 instrument (IONTOF GmbH, Münster, Germany). Negative secondary ions corresponding to elements H, D, Li, O, and Al were collected in dual-beam, non-interlaced mode. Material removal was achieved using a 2.0 keV Cs^+ sputter beam (142–128 nA), rastered over a 200 × 200 μm^2 area to produce a uniform sputter crater. For analysis, a focused 25 keV Bi^+ primary ion beam (~1.40 pA, 10 kHz repetition rate, ~5 μm spot size) was rastered over a 50 × 50 μm^2 central area (128 × 128 pixels) within the sputtered region, ensuring that data were collected from the flat-bottom portion of the crater. Each depth-profiling cycle consisted of 10.0 s of sputtering, followed by a 2.0 s pause and 3.28 s of data acquisition (two scans).

To mitigate charging during analysis, a 10 eV electron flood gun was employed for charge compensation, and a ~15 nm gold film was deposited on the pellet backside to improve conductivity and signal intensity [11]. Multiple regions were examined on each sample to verify reproducibility and exclude local inhomogeneities. Depth calibration of the sputtered craters was performed using a Veeco Dektak 150 stylus profilometer, yielding depth measurement accuracy within a few percent.

3. Results and Discussion

3.1. Microstructural features and precipitate dimensions

3.1.1. Crystal structure of tetragonal γ-$LiAlO_2$

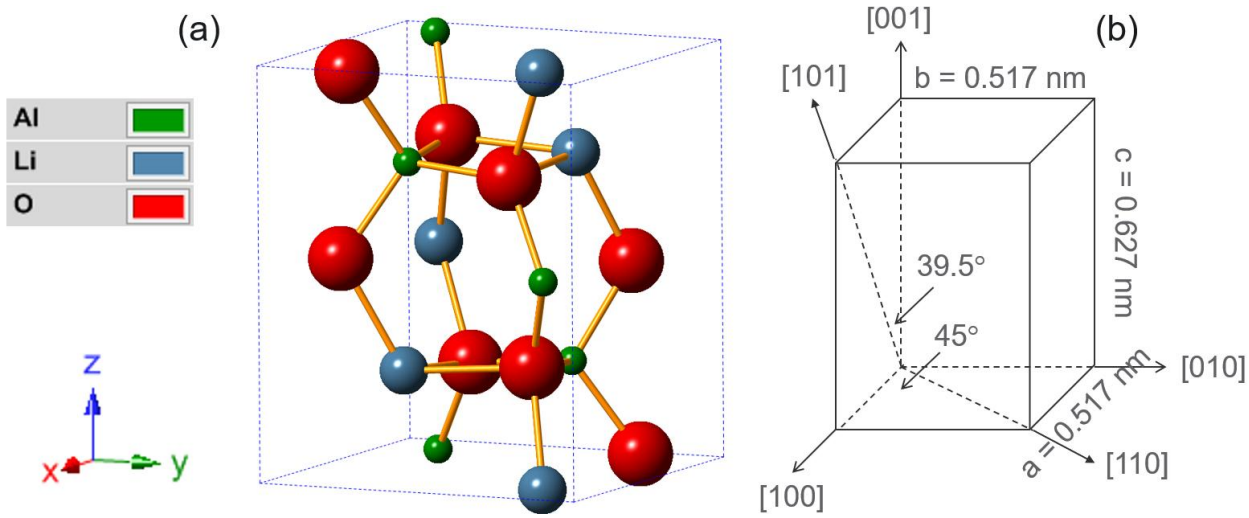

Figure 4. (a) Unit cell of the tetragonal γ-$LiAlO_2$ crystal structure, and (b) schematic for the unit cell showing crystallographic axes.

Fig. 4(a) presents the unit cell of the γ-$LiAlO_2$ crystal structure, generated using the commercial software Crystal Maker [12]. The γ-$LiAlO_2$ phase crystallizes in a tetragonal structure [space group $P4_12_12$ (No. 92)] with lattice parameters a = 0.51687 nm and c = 0.62679 nm at room temperature [13]. The angles between major crystallographic directions are illustrated in Fig. 4(b): 45° between [100] and [110], and 39.5° between [001] and [101]. The theoretical mass density of γ-$LiAlO_2$ corresponds to 2615 kg/m^3 [13] (atomic density 9.555×10^{28} at./m^3). The crystal symmetry is defined by a fourfold rotation about the [001] axis and twofold rotations about the [100], [010], and [110] axes. Notably, the [100] and [001] directions are not equivalent, nor are the [110] and [101] directions. In the transmission electron microscope (TEM) used in this study, the goniometer allows a maximum rotation of ±30°, restricting sample alignments to either [100] (and possibly [110]) or [001] (and possibly [101]). Consequently, when preparing a lift-out specimen for TEM observation, there is essentially a 50% probability to align the sample along either [100] or [001].

3.1.2. High dose-rate case

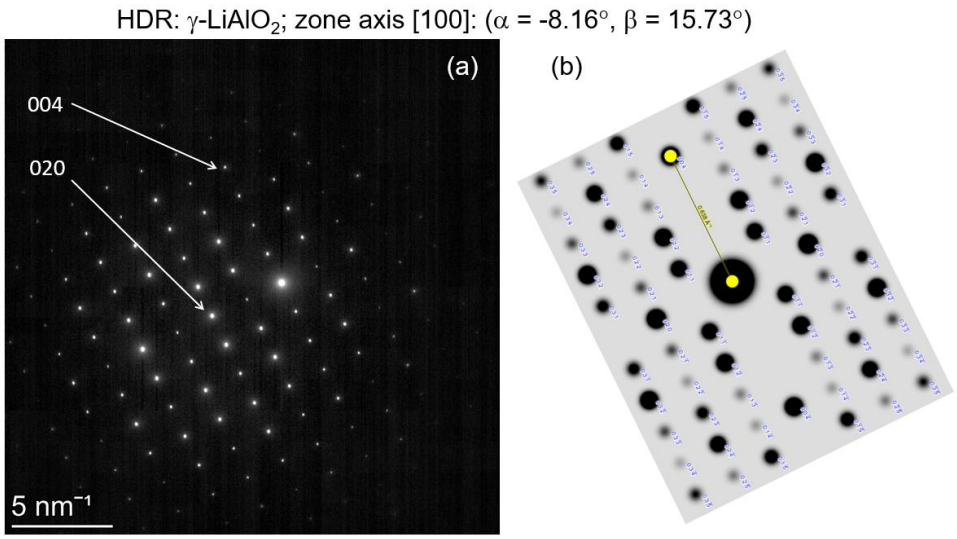

Figure 5. (a) Experimental electron diffraction pattern from γ-LiAlO$_2$ (irradiated to 2×10^{17} (He^++D^+)/cm^2 at 500 °C with a high dose rate of 7.3×10^{-4} dpa/s) along the [100] crystallographic axis. (b) The corresponding simulated diffraction pattern.

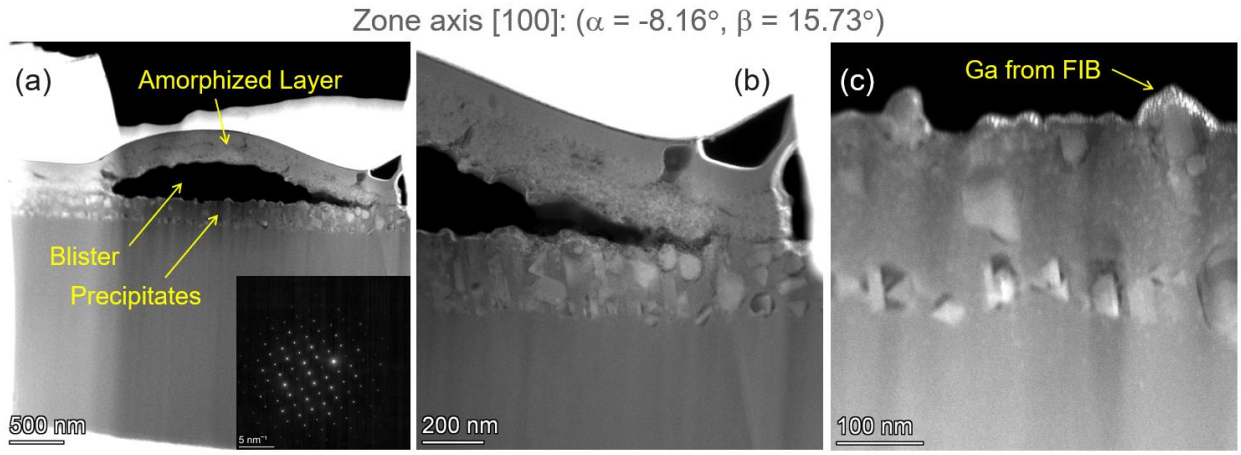

Figure 6. STEM micrographs of the microstructure of a [100]-oriented γ-LiAlO$_2$ pallet irradiated to 2×10^{17} (He^++D^+)/cm^2 at 500 °C with a high dose rate of 7.3×10^{-4} dpa/s at (a) low, (b) medium, and (c) high magnifications.

A crystalline γ-LiAlO$_2$ grain, several micrometers in size, was examined from the FIB-prepared sample irradiated to a combined fluence of 2×10^{17} (He^++D^+)/cm^2 at 500 °C, with a high dose rate of 7.3×10^{-4} dpa/s. The grain was manually oriented with the analytical electron beam in the TEM. The corresponding selected-area electron diffraction (SAED) pattern is shown in Fig. 5(a), while Fig. 5(b)

presents the simulated diffraction pattern. By matching the measured *d*-spacing values of the (004) and (020) planes with the simulation, the grain was confirmed to be aligned along the [100] zone axis.

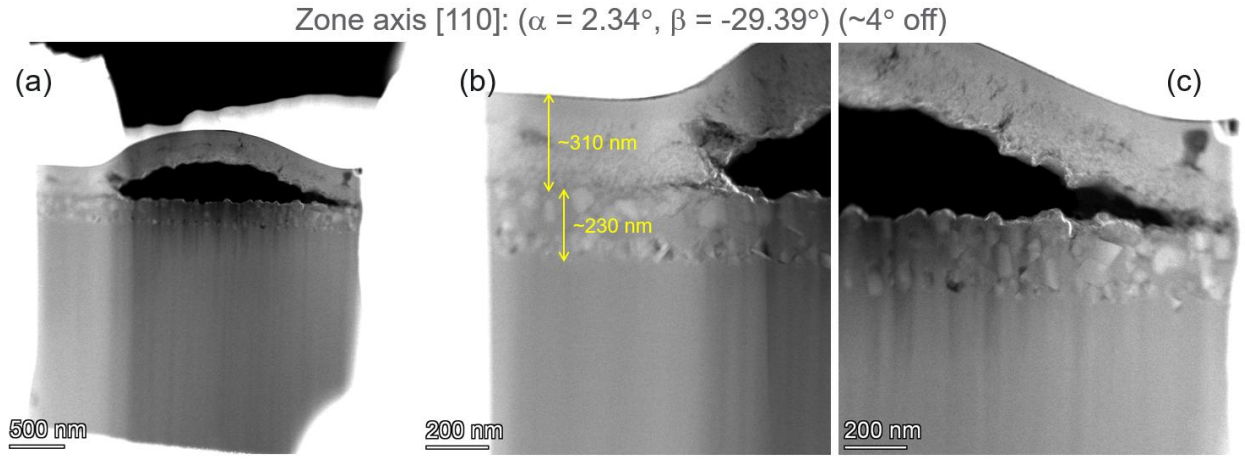

Figure 7. STEM micrographs of the microstructure of a nearly [110]-oriented γ-$LiAlO_2$ pallet irradiated to 2×10^{17} $(He^+ + D^+)/cm^2$ at 500 °C with a high dose rate of 7.3×10^{-4} dpa/s at (a) low, (b) and (c) medium magnifications.

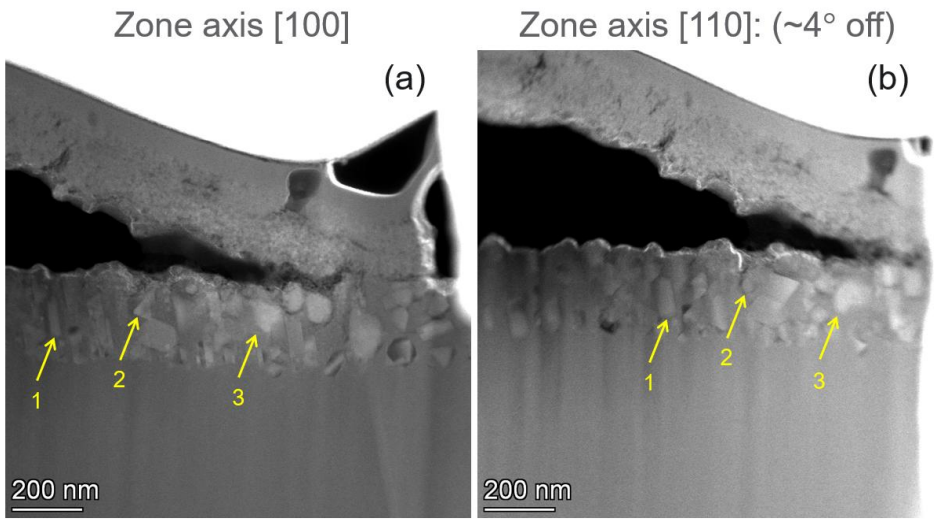

Figure 8. Comparison of the microstructures in the γ-$LiAlO_2$ pellet sample irradiated to 2×10^{17} $(He^+ + D^+)/cm^2$ at 500 °C with a high dose rate of 7.3×10^{-4} dpa/s, observed along (a) [100] and (b) [110] crystallographic axes.

Figure 6 displays the microstructural features of the irradiated grain. The imaged region contains a prominent blister ~1.7 μm in length, with the upper layer fully amorphized [Fig. 6(a)]. This amorphization is likely driven by material decomposition associated with electronic stopping in the near-surface region, where ionization and electronic excitation dominate over atomic displacements, consistent

with observations in lithium silicates [14]. Whether the amorphized layer was generated by He^+ ion irradiation prior to D_2^+ ion irradiation remains to be determined. Beneath this amorphous surface lies a crystalline region containing a dense distribution of precipitates [Fig. 6(b)]. The blister delineates these two distinct layers, with implanted gases accumulating at the interface. The curvature of the blister suggests internal pressurization from trapped gas. Minor Ga contamination introduced during FIB sample preparation is also evident [Fig. 6(c)].

An additional effort was made to orient the same grain along the [110] zone axis. Due to the goniometer's rotation angle limitations, the alignment was slightly off by ~4°, but still sufficiently close to enable meaningful observations. This small misalignment is not expected to significantly affect the shapes of microstructural features or the precipitate sizes. STEM images obtained near the [110] orientation are shown in Fig. 7. Similar microstructural features are evident as those observed along [100], including the surface blister, amorphized layer, and precipitate-rich crystalline region.

A comparison of the same region imaged along [100] and [110] zone axes is presented in Fig. 8. The arrows labeled 1, 2, and 3 mark identical precipitates observed from the two orientations. As expected, the apparent size and shape of each precipitate vary with imaging direction, highlighting the three-dimensional nature and asymmetry of these features.

3.1.3. Medium dose-rate case

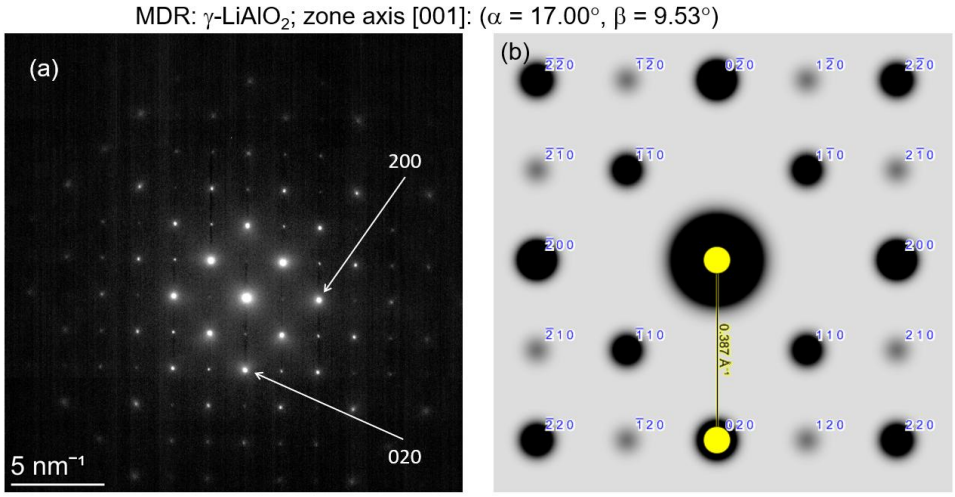

Figure 9. (a) Experimental electron diffraction pattern from γ-$LiAlO_2$ (irradiated to 2×10^{17} $(He^+ + D^+)/cm^2$ at 500 °C with a medium dose rate of 2.9×10^{-4} dpa/s) along the [001] crystallographic axis. (b) The corresponding simulated diffraction pattern.

A similar alignment procedure was applied on a crystalline γ-$LiAlO_2$ grain in the FIB sample irradiated to a combined fluence of 2×10^{17} $(He^+ + D^+)/cm^2$ at 500 °C, with a medium dose rate of 2.9×10^{-4} dpa/s. The grain was oriented along the [001] zone axis from the diffraction pattern as shown in Fig. 9. In tetragonal γ-$LiAlO_2$, [001] and [100] are perpendicular and not crystallographically equivalent. It is not possible to access both orientations within a single FIB lamella.

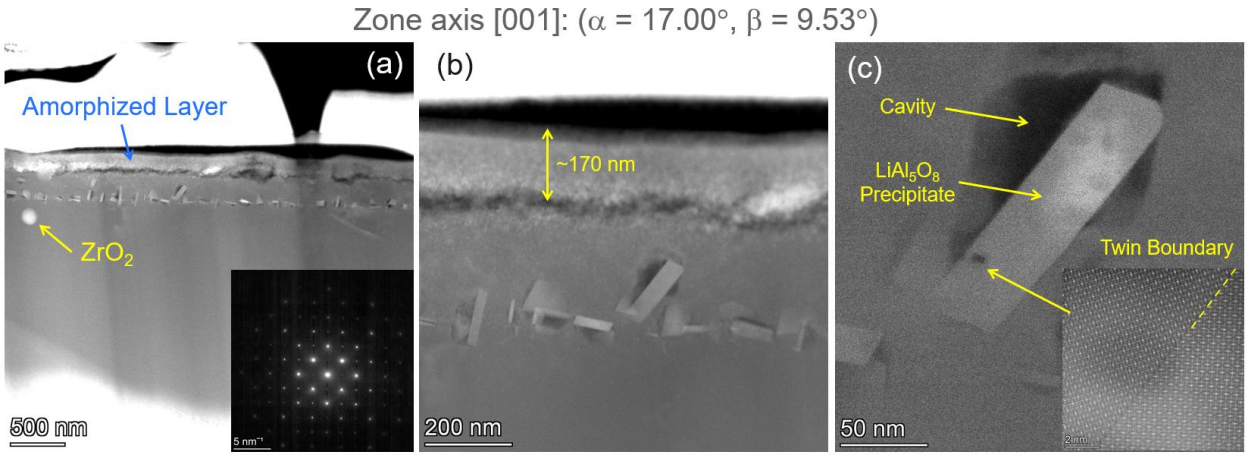

Figure 10. STEM micrographs of the microstructure of a [001]-oriented γ-$LiAlO_2$ pallet irradiated to 2×10^{17} (He^++D^+)/cm^2 at 500 °C with a medium dose rate of 2.9×10^{-4} dpa/s at (a) low, (b) medium, and (c) high magnifications.

The corresponding microstructure of the irradiated region is shown in Fig. 10. Similar to the high dose-rate sample, the region exhibits a three-layered morphology consisting of an amorphous surface layer, a subsurface zone enriched with implanted gas, and an underlying crystalline region containing precipitates. However, the amorphized layer in this case is noticeably thinner (~170 nm) compared to the high dose-rate condition [~310 nm in Fig. 7(b)]. The underlying causes for this difference are not yet fully understood, but several possibilities may be considered: (1) a reduced rate of electronic energy deposition under the medium dose-rate conditions may decrease the amorphization probability for a given electronic stopping power, (2) preferential amorphization along a specific crystallographic direction in γ-$LiAlO_2$ could lead to thickness variations depending on the observation zone axis, and (3) different ion fluences or irradiation temperatures due to fluctuations during the experiment could affect the thickness, though the latter is considered less likely.

Unlike the high dose-rate case, the gas-enriched interface in the medium dose-rate sample does not display a fully developed blister morphology such as that observed in Fig. 6. Nevertheless, this absence does not necessarily preclude blister formation, as similar features may exist in regions outside of the areas examined. Atomic-level resolution imaging of the precipitate reveals a spinel-like crystal structure containing a well-defined twin boundary, most likely aligned with a {111} crystallographic plane. This observation is consistent with previously established orientation relationships between the $LiAl_5O_8$ precipitates and the γ-$LiAlO_2$ matrix [5,15], namely $LiAl_5O_8$ [111] // γ-$LiAlO_2$ [100] and $LiAl_5O_8$ $(2\bar{2}0)$ // γ-$LiAlO_2$ (001). Based on these relationships, the [100] axis of γ-$LiAlO_2$ lies within the image plane and is oriented perpendicular to the precipitate's long side, while the [010] axis is parallel to it.

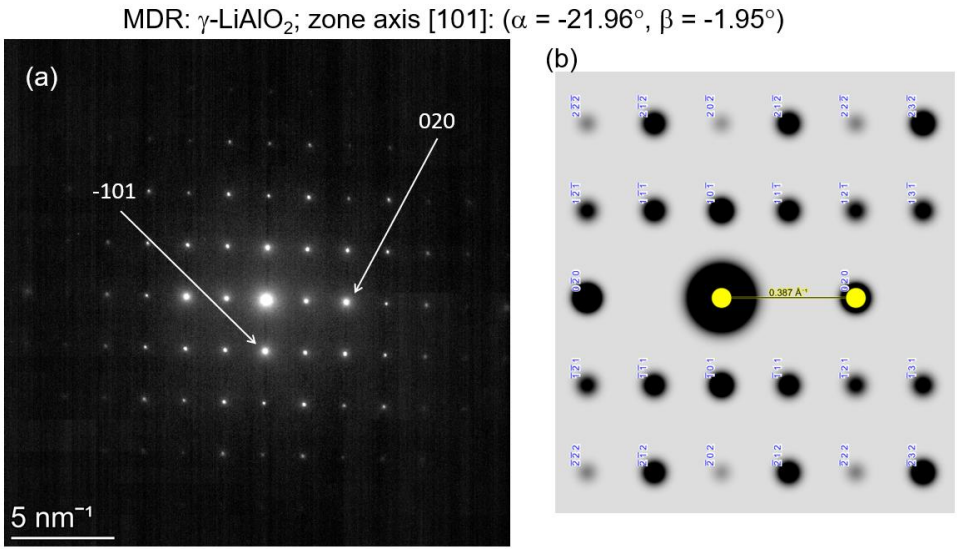

Figure 11. (a) Experimental electron diffraction pattern from γ-$LiAlO_2$ (irradiated to 2×10^{17} $(He^+ + D^+)/cm^2$ at 500 °C with a medium dose rate of 2.9×10^{-4} dpa/s) along the [101] crystallographic axis. (b) The corresponding simulated diffraction pattern.

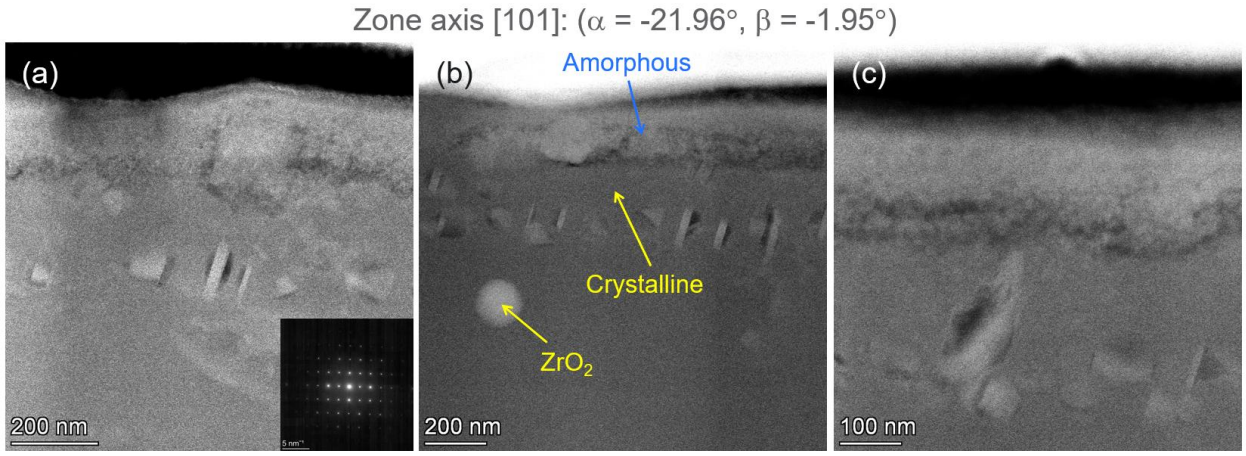

Figure 12. STEM micrographs of the microstructure of a [101]-oriented γ-$LiAlO_2$ pallet irradiated at 500 °C to 2×10^{17} $(He^+ + D^+)/cm^2$ at a medium dose rate of 2.9×10^{-4} dpa/s at (a) and (b) medium and (c) high magnifications.

The same grain was also aligned under TEM along the [101] zone axis, as shown in Fig. 11, and its corresponding microstructure is presented in Fig. 12. Similar features are observed from this orientation, consistent with those in Fig. 10. The spherical particle visible in Fig. 12(b) is identified as ZrO_2, introduced as an impurity during the pellet fabrication process.

3.1.4. Low dose-rate case

Figure 13(a) presents the experimental electron diffraction pattern acquired from a crystalline γ-LiAlO$_2$ grain within the FIB-prepared sample irradiated to a combined fluence of 2×10^{17} (He^++D^+)/cm^2 at 500 °C under a low dose rate of 6.8×10^{-5} dpa/s. The corresponding simulated diffraction pattern, shown in Fig. 13(b), confirms that the grain is aligned along the [100] zone axis.

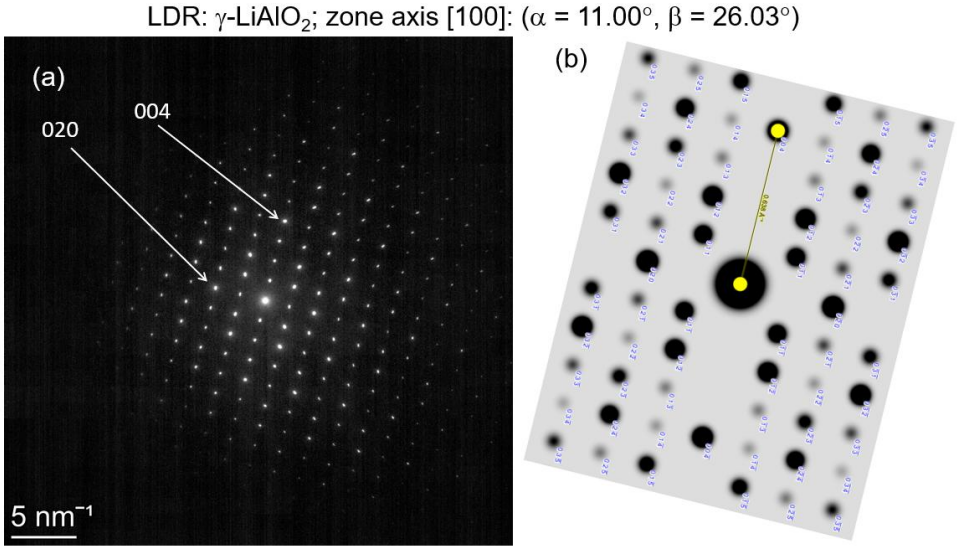

Figure 13. (a) Experimental electron diffraction pattern from γ-LiAlO$_2$ (irradiated to 2×10^{17} (He^++D^+)/cm^2 at 500 °C with a low dose rate of 6.8×10^{-5} dpa/s) along the [100] crystallographic axis. (b) The corresponding simulated diffraction pattern.

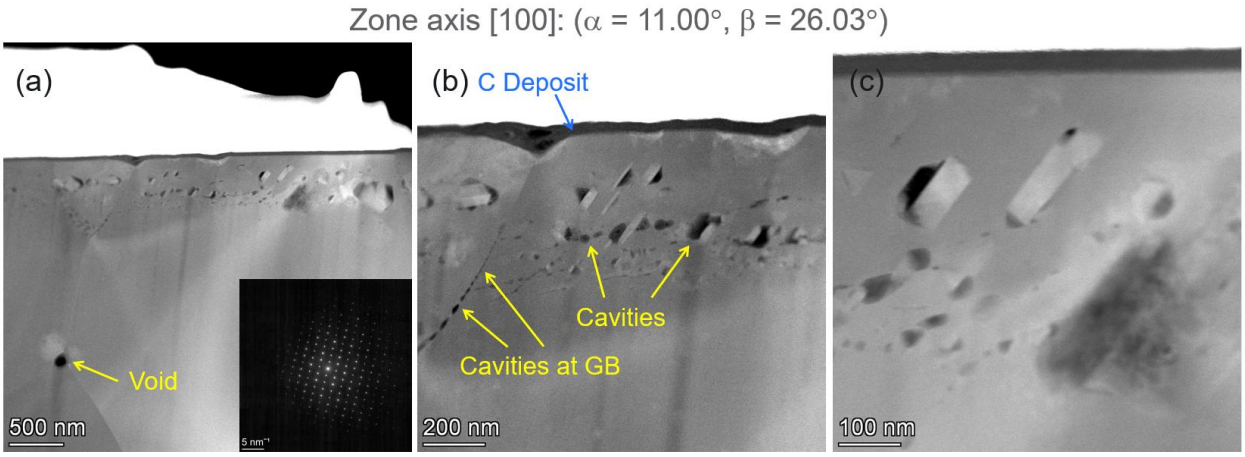

Figure 14. STEM micrographs of the microstructure of a [100]-oriented γ-LiAlO$_2$ pallet irradiated to 2×10^{17} (He^++D^+)/cm^2 at 500 °C with a low dose rate of 6.8×10^{-5} dpa/s at (a) low, (b) medium, and (c) high magnifications.

Figure 14 illustrates the microstructure of the irradiated region at multiple magnifications. In contrast to samples irradiated at medium and high dose rates, no complete amorphization is observed across the irradiated layer. Instead, the region remains crystalline, and there is no distinct depth at which preferential gas accumulation occurs. Precipitates are distributed in the crystalline γ-LiAlO$_2$ matrix, accompanied by both rectangular and triangular cavities corresponding to different crystallographic orientations. Cavities are observed along grain boundaries, surrounding precipitates, and within the matrix.

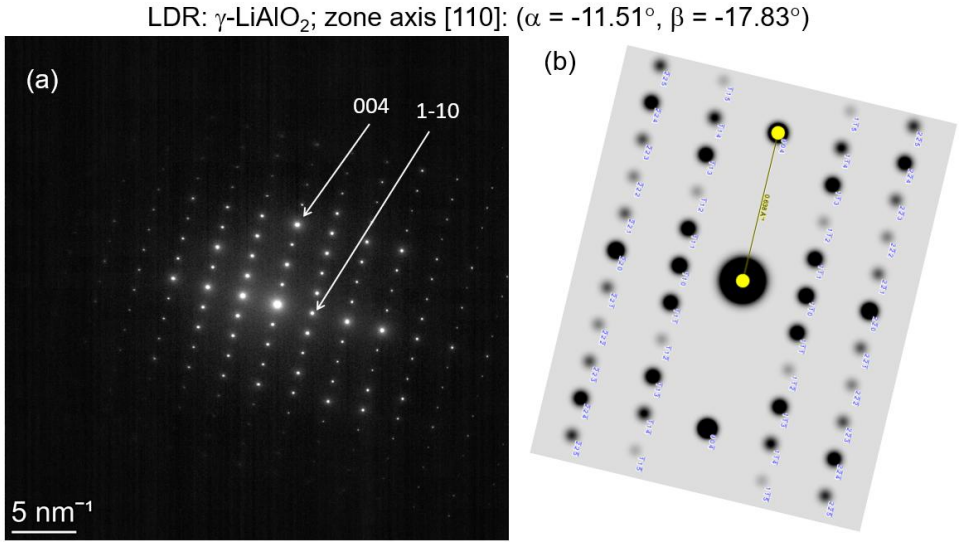

Figure 15. (a) Experimental electron diffraction pattern from γ-LiAlO$_2$ (irradiated to 2×10^{17} $(He^+ + D^+)/cm^2$ at 500 °C with a low dose rate of 6.8×10^{-5} dpa/s) along the [110] crystallographic axis. (b) The corresponding simulated diffraction pattern.

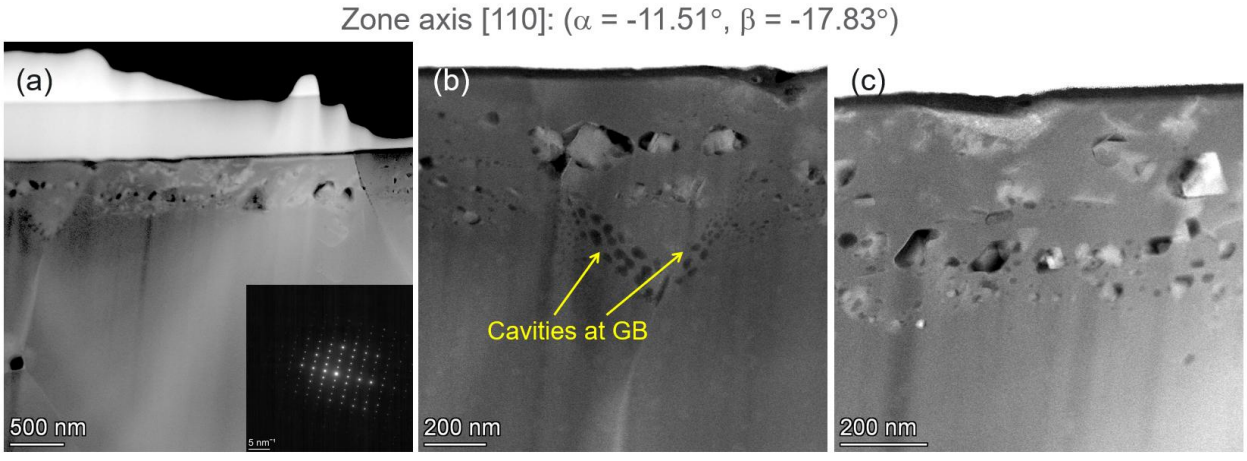

Figure 16. STEM micrographs of the microstructure of a [110]-oriented γ-LiAlO$_2$ pallet irradiated to 2×10^{17} $(He^+ + D^+)/cm^2$ at 500 °C with a low dose rate of 6.8×10^{-5} dpa/s at (a) low, (b) and (c) medium magnifications.

Additional characterization was performed with the grain aligned along the [110] zone axis, as shown in Fig. 15, corresponding to a 45° rotation relative to [100]. The microstructure observed along [110] (Fig. 16) reveals features consistent with those seen along [100], including aggregated cavities prominently decorating the grain boundary plane. The clear visibility of these cavities along the off-edge viewing direction indicates a preferential tendency for cavities to nucleate and grow along grain boundaries.

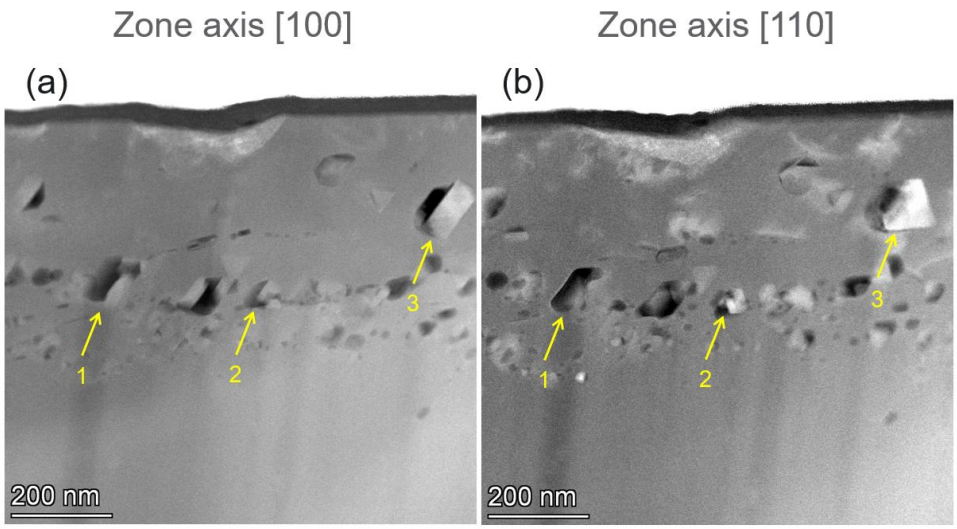

Figure 17. Comparison of the microstructures in the γ-$LiAlO_2$ pellet sample irradiated to 2×10^{17} $(He^+ + D^+)/cm^2$ at 500 °C with a low dose rate of 6.8×10^{-5} dpa/s, observed along the (a) [100] and (b) [110] crystallographic axes.

To further examine the three-dimensional morphology of the precipitates and cavities, Fig. 17 compares microstructural images acquired along both orientations, with arrows marking selected precipitates for reference. Upon rotating the grain by 45° from [100] to [110], each precipitate exhibits a change in apparent shape and projected size due to the different crystallographic viewing directions. For example, precipitate 3 transforms from a rectangular morphology when viewed along [100] to a triangular morphology along [110]. Such shape changes highlight the anisotropic geometry of the precipitates and demonstrate the importance of multi-orientation imaging for accurately assessing their morphology and spatial distribution.

3.1.5. Comparison of microstructure and precipitate size

For comparison of irradiation effects, Fig. 18 presents the microstructures of γ-$LiAlO_2$ grains irradiated to a combined fluence of 2×10^{17} $(He^+ + D^+)/cm^2$ at 500 °C under three different dose rates, with observations taken along both the [100] and [001] zone axes. The microstructures of the low- and high-dose-rate samples observed along [100] [Figs. 18(a) and 18(b)] allow a direct comparison. However, the medium-dose-rate sample was examined along [001] [Fig. 18(c)], which limits direct comparison due to crystallographic orientation differences. Further efforts will be made to obtain corresponding data along the [100] zone axis.

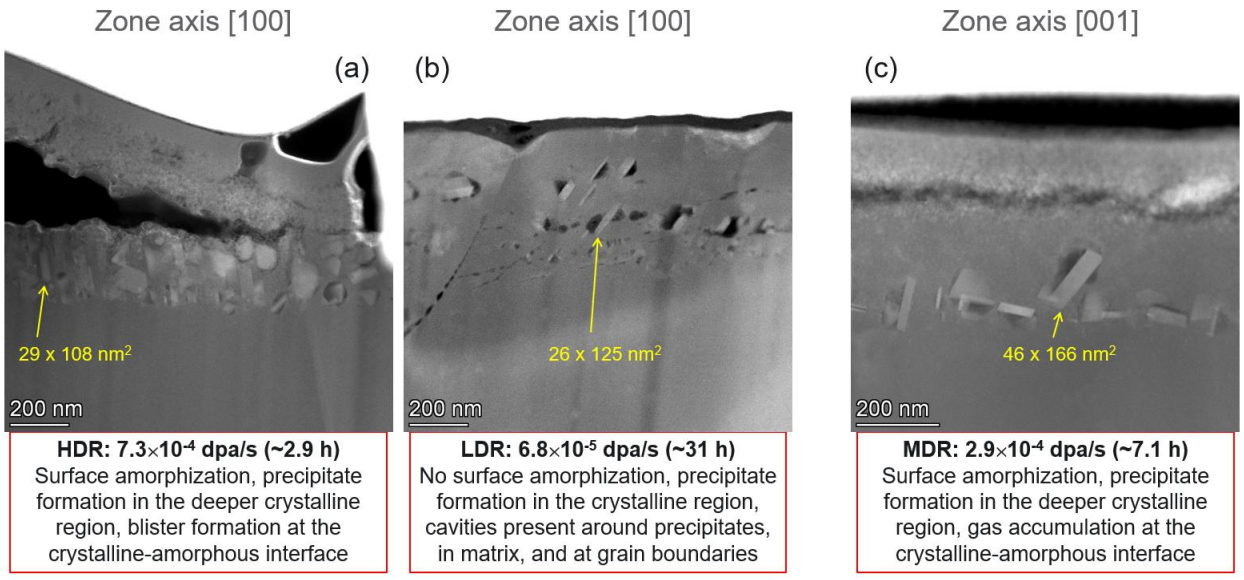

Figure 18. STEM micrographs of the microstructures of [100]- and [001]-oriented γ-$LiAlO_2$ pallets irradiated to 2×10^{17} $(He^+ + D^+)/cm^2$ at 500 °C with dose rates of (a) 7.3×10^{-4}, (b) 6.8×10^{-5}, and (c) 2.9×10^{-4} dpa/s, corresponding to irradiation times of ~2.9, ~31 and ~7.1 h, respectively.

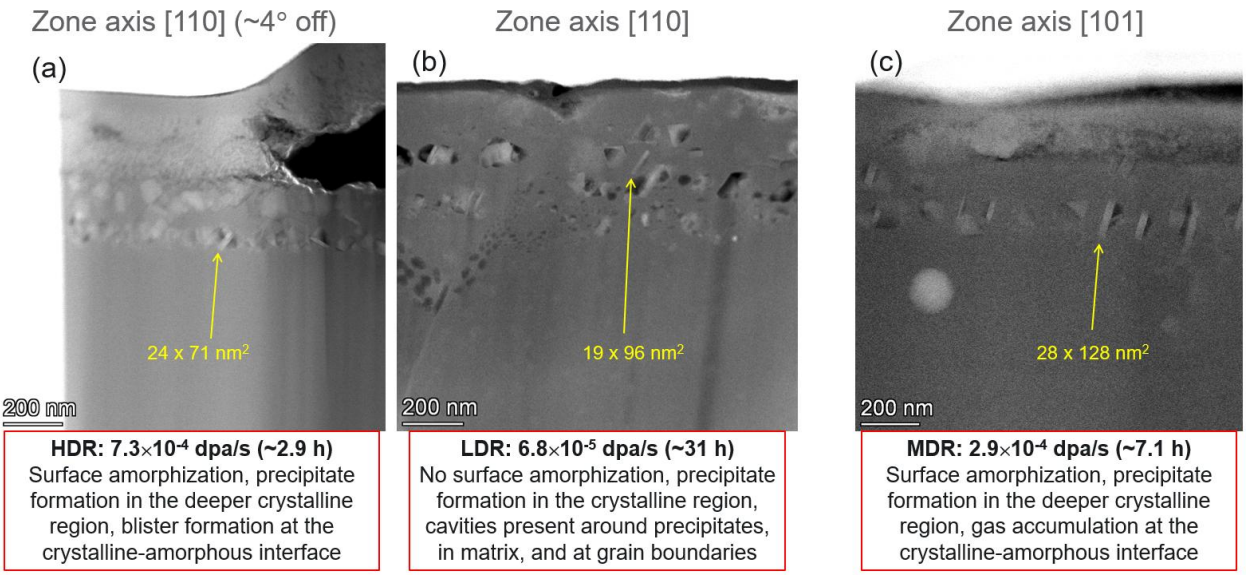

Figure 19. STEM micrographs of the microstructures of [110]- and [101]-oriented γ-$LiAlO_2$ pallets irradiated to 2×10^{17} $(He^+ + D^+)/cm^2$ at 500 °C with dose rates of (a) 7.3×10^{-4}, (b) 6.8×10^{-5}, and (c) 2.9×10^{-4} dpa/s, corresponding to irradiation times of ~2.9, ~31 and ~7.1 h, respectively.

Quantitative measurements of precipitate size show typical projected dimensions of ~29 × 108 nm^2 for the high-dose-rate sample and ~26 × 125 nm^2 for the low-dose-rate sample [Figs. 18(a) and 18(b)],

indicating that within this dose-rate range, the effect on precipitate size is relatively minor. However, the similarity in precipitate size does not necessarily imply that further reductions in dose rate would have no effect. In fact, irradiation of γ-$LiAlO_2$ under a thermalized fission neutron spectrum at 300 °C, with dose rates ~2–3 orders of magnitude lower, produced micron-sized precipitates. This suggests that precipitate size may not scale linearly with dose rate within the regime explored in this study.

In contrast, the precipitates in the medium-dose-rate sample appear slightly larger, with an average size of ~46 × 166 nm^2 [Fig. 18(c)]. This apparent size difference is likely associated with anisotropic precipitate growth rates along different crystallographic directions in tetragonal γ-$LiAlO_2$, rather than solely a dose-rate effect.

Moreover, dose rate appears to influence the mobility and distribution of implanted gas species. At the low dose rate, gas accumulation is more dispersed, with isolated, likely gas-filled cavities forming at various locations, including within the matrix, surrounding precipitates, and along grain boundaries. In contrast, at the high dose rate, implanted gas atoms tend to migrate and accumulate preferentially near the crystalline–amorphous interface, leading to the formation of larger blisters or aggregated cavities. This observation implies enhanced diffusion kinetics of implanted gases at higher dose rates.

A comparison of microstructures along or near the [110] axis is shown in Figs. 19(a) and 19(b). The same general trends are observed: the high- and low-dose-rate samples exhibit comparable precipitate sizes, whereas the medium-dose-rate sample again shows slightly larger precipitates along [101].

3.2. Deuterium retention and lithium loss

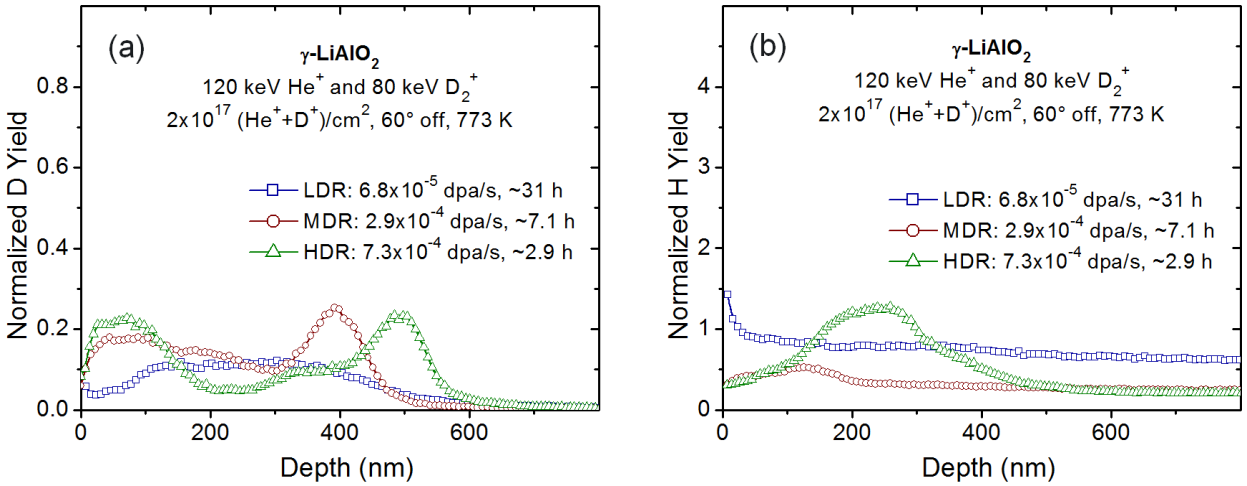

Figure 20. ToF-SIMS depth profiles of normalized (a) D/Al and (b) H/Al yields in γ-$LiAlO_2$ pellets irradiated to 2×10^{17} $(He^+ + D^+)/cm^2$ at 500 °C with dose rates of 6.8×10^{-5}, 2.9×10^{-4} and 7.3×10^{-4} dpa/s.

Fig. 20 presents the normalized ToF-SIMS depth profiles of D and H, shown relative to Al yields, in γ-$LiAlO_2$ pellets irradiated to a combined fluence of 2×10^{17} $(He^+ + D^+)/cm^2$ at 500 °C under three different dose rates. In this analysis, it is assumed that Al yields remain constant throughout the depth, thereby

serving as a stable reference for yield normalization. It is important to note that ToF-SIMS selectively detects atomic deuterium trapped within the microstructure, whereas molecular D_2 gas confined in cavities can escape immediately into the vacuum upon sputtering-induced rupture and may therefore not be effectively detected.

At the high dose rate of 7.3×10^{-4} dpa/s, the D depth profile exhibits a distinct double-peak structure [Fig. 20(a)], accompanied by a corresponding H peak at the same depth [Fig. 20(b)]. This correlated behavior is attributed to isotopic exchange between H and D, a phenomenon previously observed in sequential ion irradiation experiments of γ-LiAlO$_2$ pellets [3]. Isotopic exchange is a reversible chemical process in which isotopes are exchanged between ions or molecules without an associated energy difference. Such exchange has also been reported to enhance tritium release during neutron irradiation through H–T isotopic exchange.

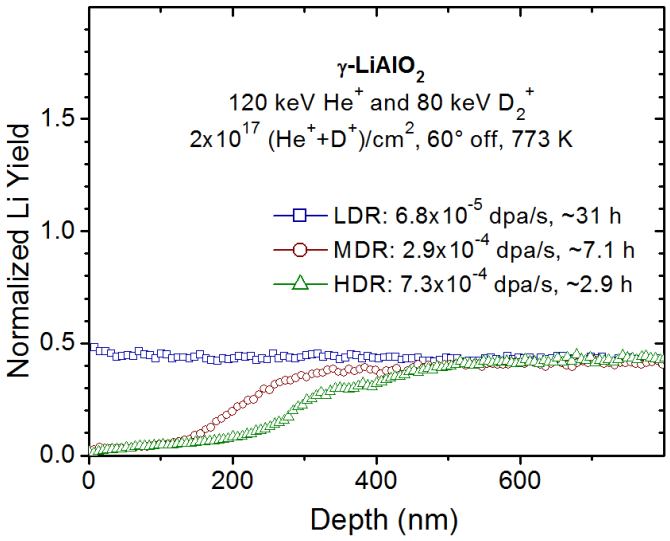

Figure 21. ToF-SIMS depth profiles of normalized Li/Al yields in γ-LiAlO$_2$ pellets irradiated to 2×10^{17} $(He^+ + D^+)/cm^2$ at 500 °C with dose rates of 6.8×10^{-5}, 2.9×10^{-4} and 7.3×10^{-4} dpa/s.

The influence of dose rate on isotopic exchange is evident when comparing different irradiation conditions. At the high dose rate, the rapid buildup of D concentration creates a localized peak where isotopic exchange is most likely to occur, leading to the observed double-peak structure. In contrast, at lower dose rates, isotopic exchange is minimal throughout the irradiated depth. This behavior likely arises from the slower accumulation of D concentration, which reduces the probability of trapped D being exchanged with mobile H from the environment at 500 °C.

Fig. 21 shows the normalized Li/Al yields as a function of depth for the same samples. At the high dose rate of 7.3×10^{-4} dpa/s, significant Li loss is observed during irradiation, extending from the surface to a depth of ~300 nm, mainly within the amorphized surface region [Fig. 7(b)]. At the medium dose rate of 2.9×10^{-4} dpa/s, Li depletion is less pronounced and largely confined to the amorphized surface layer [Fig. 10(b)]. These results are consistent with earlier observations of Li loss in γ-LiAlO$_2$ pellets irradiated

at 500 °C [15,16]. In contrast, the low dose-rate sample (6.8×10^{-5} dpa/s) exhibits no measurable Li loss and no surface amorphization.

4. Conclusions

This study systematically investigated the microstructural evolution, deuterium retention, and lithium loss in γ-$LiAlO_2$ pellets irradiated to a combined fluence of 2×10^{17} $(He^+ + D^+)/cm^2$ at 500 °C under three different dose rates of 7.3×10^{-4}, 2.9×10^{-4} and 6.8×10^{-5} dpa/s. The major conclusions are as follows:

- At medium and high dose rates, the irradiated regions developed a surface amorphized layer, beneath which implanted gas accumulated and large blisters developed at the crystalline–amorphous interface. Precipitates were observed in the crystalline region. Further investigation is needed to determine whether the amorphized layer originated from He^+ ion irradiation preceding the D_2^+ ion irradiation.
- At the low dose rate, the material remained crystalline, with cavities distributed around precipitates, within the matrix, and along grain boundaries. These findings suggest that higher dose rates may enhance gas transport during irradiation.
- Projected precipitate sizes were comparable between high- and low-dose-rate samples along [100] or [110] zone axes. The weak dependence of precipitate size on dose rate within the studied range does not necessarily rule out an effect at lower dose rates.
- Slightly larger precipitates were observed in the medium-dose-rate sample along the [001] and [101] axes compared to those in the high- or low-dose-rate samples along [100] and [110]. This difference is likely due to anisotropic precipitate growth rates along specific crystallographic directions in tetragonal γ-$LiAlO_2$, rather than solely a dose-rate effect.
- At the low dose rate, isotopic exchange between mobile H and trapped D was minimal throughout the irradiated depth region.
- At the high dose rate, the D profile exhibited a double-peak structure accompanied by an H peak at the D-profile minimum, indicating enhanced isotopic exchange between H and D.
- No measurable Li loss was detected in the low-dose-rate sample, which did not develop an amorphized layer.
- At medium and high dose rates, Li loss from the amorphized surface region increased with dose rate, suggesting enhanced Li out-diffusion.

In summary, dose rate has a critical impact on amorphization, gas redistribution, and Li depletion in γ-$LiAlO_2$. These results offer important insights into the coupled processes of defect generation, Li and gas transport, and isotopic exchange, advancing the understanding of γ-$LiAlO_2$ as a tritium breeding material under reactor-relevant irradiation conditions.

5. Acknowledgments

This work was supported by Tritium Modernization Program, sponsored by National Nuclear Security Administration, U.S. Department of Energy. Ion irradiation experiments were performed at Texas A&M University, and sample characterizations were conducted at PNNL.

6. References

[1] W. Jiang, S.R. Spurgeon, Z. Zhu, X. Yu, K. Kruska, T. Wang, J. Gigax, L. Shao, D.J. Senor, J. Nucl. Mater. 511 (2018) 1.
[2] W. Jiang, L. Kovarik, M.G. Wirth, Z. Zhu, Z. Hu, L. Shao, A.M. Casella, D.J Senor, J. Nucl. Mater. 591 (2024) 154925.
[3] W. Jiang, T. Wang, Y. Wang, Z. Zhu, L. Shao, D.J. Senor, J. Nucl. Mater. 538 (2020) 152357.
[4] W. Jiang, W.G. Luscher, T. Wang, Z. Zhu, L. Shao, D.J. Senor, J. Nucl. Mater. 542 (2020) 152532.
[5] W. Jiang, L. Kovarik, Z. Zhu, T. Varga, M.E. Bowden, B.E. Matthews, Z. Hu, L. Shao, D.J Senor, J. Appl. Phys. 131 (2022) 215902.
[6] W. Jiang, A.M. Casella, D.J. Senor, *Effects of irradiation temperature on the microstructure and deuterium retention in γ-$LiAlO_2$ pellets*, PNNL-36560, September 2024.
[7] S. Dudarev, K. Arakawa, X. Yi, Z. Yao, M.L. Jenkins, M.R. Gilbert, P.M. Derlet, J. Nucl. Mater. 455 (2014) 16.
[8] W. Jiang, Y. Zhu, L. Zhang, D.J. Edwards, N.R. Overman, G. Nandipati, W. Setyawan, C.H. Henager Jr., R.J. Kurtz, J. Nucl. Mater. 550 (2021) 152905.
[9] J.F. Ziegler, J.P. Biearsack, U. Littmark, *The stopping and Range of Ions in Solids* (Pergamon Press, New York, 1985); available at: http://www.SRIM.org/.
[10] H. Tsuchihira, T. Oda, and S. Tanaka, Nucl. Instr. Meth. Phys. Res. B 269 (2011) 1707.
[11] Y. Zhou, M. Xia, V. Suseela, H.M. Kao, R.M. Asmussen, A. Bhattacharjee, C.A. Creamer, M. Liu, J.G. Wang, Z. Zhu, Anal. Chem. 97 (2025) 8755.
[12] Crystal and Molecular Structures Modeling & Diffraction, CrystalMaker Software Ltd., http://www.crystalmaker.com.
[13] M. Marezio, Acta Cryst. 19 (1965) 396.
[14] W. Jiang, L. Kovarik, M.G. Wirth, Z. Zhu, N.L. Canfield, L.M. Seymour, L/M. Bagaasen, M.E. Bowden, T. Varga, N.R. Overman, Z. Hu, L. Shao, D.J. Senor, J. Nucl. Mater. 576 (2023) 154281.
[15] W. Jiang, J. Zhang, L. Kovarik, Z. Zhu, L. Price, J. Gigax, E. Castanon, X. Wang, L. Shao, D.J. Senor, J. Nucl. Mater. 484 (2017) 374.
[16] W. Jiang, J. Zhang, D.J. Edwards, N.R. Overman, Z. Zhu, L. Price, J. Gigax, E. Castanon, L. Shao, D.J. Senor, J. Nucl. Mater. 494 (2017) 411.